Catalytic micro-structured ceramic beads and efficacy evaluation through SMX degradation in PMS-activated systems

Jiaojiao Zheng [a], Hongqi Sun [b], Kang Li [c], Zhentao Wu [a,*]

[a] *Energy and Bioproducts Research Institute (EBRI), Aston University, Birmingham B4 7ET, UK*
[b] *School of Molecular Sciences, The University of Western Australia, 35 Stirling Highway, Perth, WA 6009, Australia*
[c] *Barrer Centre, Department of Chemical Engineering, Imperial College London, London SW7 2AZ, UK*

ARTICLE INFO

ABSTRACT

This study tackles the challenge of applying fine and nano-catalyst particles in Advanced Oxidation Processes (AOPs), primarily due to the complexities of nanoparticle removal from treated water to prevent secondary nano-hazards. We propose an innovative solution: micro-structured ceramic beads (MSCBs, approximately 3 mm in diameter) with a unique anisotropic pore structure. For the first time, we prepared MSCBs impregnated with cobalt oxide (Co/MSCBs) using a phase-inversion and sintering-assisted process. The Co/MSCBs were investigated for the degradation of sulfamethoxazole (SMX) in the peroxymonosulfate (PMS) induced AOPs system under mild reaction conditions. The effects of operating parameters (e.g., SMX concentration, reaction temperature, and catalyst dosage) in the Co/MSCBs|PMS system were studied on three different types of catalytic ceramic beads: 2Co/MSCB0 (beads with a common isotropic pore structure), 2Co/MSCB1 (beads with radial finger-like microstructures and a denser outer skin-layer), and 2Co/MSCB2 (beads with finger-like microstructures and no outer skin layer). At 20 °C, 2Co/MSCB2 (59.1 %) demonstrated a higher degradation efficiency for 40 mg/L SMX in comparison to 2Co/MSCB1 (54.9 %) and 2Co/MSCB0 (49.6 %). Additionally, it is noteworthy that the sample 2Co/MSCB2, after being used and regenerated, exhibited significantly a higher catalytic performance (70.83 % removal in 20 min during the 16th run) than the fresh one (70.47 % removal in 120 min). After reactions, Co/MSCBs can be readily separated from the bulk solution and used for the next run, making them ideal for practical applications. Furthermore, a radical quenching experiment was conducted, and a plausible catalytic mechanism was proposed. This research presents a new approach for the fabrication of micro-structured ceramic beads that are capable of effectively overcoming the diffusion limitations encountered in both heterogeneous reactions and adsorption processes.

1. Introduction

Environmental pollution arising from pharmaceutical and personal care products that include but are not limited to antibiotics, antimicrobial agents, cosmetics, etc. has been attracting a great deal of attention in recent years [1,2]. Sulfamethoxazole (SMX) is a typical sulphonamide antibiotic drug widely used against human and veterinary infections, but recalcitrant to conventional wastewater treatment plants due to its strong hydrophilicity, high stability, and antibacterial nature [3,4]. Continuous exposure or the accumulation of SMX in a long term could pose an adverse threat to human and public health, as well as ecosystem, for instance, chronic diseases and genetic mutation [5,6].

Sulphate radical-based advanced oxidation processes (SR-AOPs) stand as a preferred option to mitigate antibiotic contaminants due to their potential to degrade organic pollutants into non-toxic or low-toxic small molecules in water bodies. This can be attributed to the generation of highly reactive species, such as sulphate radical ($SO_4^{\cdot-}$, 2.5–3.1 V vs. NHE) and reactive oxygen species (ROS), generated by peroxymonosulfate (PMS, HSO_5^-) or persulfate (PS, $S_2O_8^{2-}$) under heat, ultrasounds, transition metal ions/oxides or UV light [3,7]. In fact, PMS (also known as Oxone®) displays a more efficient catalytic performance for the degradation of organic pollutants than PS. It has received more attention because of its high reactivity, resulting from an asymmetric structure ($HO\text{-}O\text{-}SO_3^-$) and favourable large length of the O-O bond (1.326 Å) that needs less energy to break. It goes without saying that this characteristic facilitates the activation processes under normal

---

temperature and over a wide range of pH values (2.0–8.0) to generate ROS, such as $\cdot$OH and $^1O_2$ [4,8,9]. A viable and economically feasible technique within SR-AOPs is the activation of PMS by transition metal-mediated heterogeneous catalysts to generate $SO_4^{\cdot-}$ and ROS, including the radical pathway ($SO_4^{\cdot-}$, $OH^{\cdot}$, and $\cdot O_2^{-}$) and the non-radical pathway ($^1O_2$) for the powerful pollutant treatment.

Cobalt-based catalyst, particularly cobalt oxide (Co_3O_4), is one of the most active transition metal-based catalysts in PMS activation [10,11]. However, non-immobilised Co_3O_4 catalysts usually suffer from uneven dispersion and agglomeration in water, which in turn limit the electron transfer rate and the overall catalytic activity [12]. As a result, exposing more active sites on the stable substrates is a promising strategy to improve the cobalt dispersion and stability, other than its separation from the treated water. Various materials, such as carbon-based materials, metal oxide, and zeolites have been employed as the substrates and have shown encouraging results [13–17]. Macias-Quiroga et al. reported that carbon-based catalysts (68.5 %) constitute the primary catalysts and/or catalytic supports used in AOPs, followed by TiO_2 (20.4 %), SiO_2 (5.2 %), Pillared Interlayered Clays (3.1 %), Al_2O_3 (1.6 %) and zeolites (1.2 %) [18]. Al_2O_3 accounted for a small proportion although it is one of the most common and robust substrates with an extremely high mechanical strength, thermal and chemical stability under rigorous conditions [19]. Furthermore, researchers often focus on loading catalysts onto Al_2O_3 powder for AOPs reactions, particularly γ-Al_2O_3. This is because it has a large specific surface area, although it is less stable compared to α-Al_2O_3 [19–21]. Nevertheless, it remains a difficulty to separate the used catalyst powders from the treated water, leading to the potential release of nanoparticles into the environment and resulting in secondary pollution.

The use of powdered catalysts also presents challenges for the upscaling of AOPs and other catalytic reaction processes in industrial applications, particularly within packed-bed reactors. While the use of fine powders ensures good access to catalyst active sites and reduces diffusional mass-transfer resistance, industry more commonly employs catalyst pellets of millimetre size. This approach helps mitigate the pressure drop issues associated with fine powders. However, these relatively large spheres suffer from diffusion limitation issues, making the distribution of active sites critical. As depicted in Fig. 1, conventional Al_2O_3 beads, along with other alternatives in this size range of several millimetres, are either of the homogeneous type (uniform macroscopic distribution of catalysts) or the eggshell type (non-uniform macroscopic distribution of catalysts). Technically, homogeneous-type

catalysts experience a severe mass transfer resistance inside the bulk region of Al_2O_3 beads. The degree of mass-transfer limitations in the catalytic system can be described by the Thiele modulus, denoted as φ:

$$\varphi = \frac{V_P}{A_P} \sqrt{\frac{k_r}{D_e}} \qquad (1)$$

where V_P is the volume of the catalyst support/beads, A_P is the external surface area of the catalyst support/beads, k_r is the first-order rate constant, and D_e is the effective diffusion coefficient [22]. When φ is greater than 0.3, the diffusion of the reactant through the pores is considered as reaction rate limited. As a result, a homogeneous distribution of the active phase in large catalyst supports is only beneficial for relatively slow catalytic processes that allow reactants to diffuse to the active sites. Otherwise, the catalytic reaction ends up being internally diffusion-limited when φ increases to 3 or higher. To address this, a non-uniform macroscopic distribution of catalyst patterns, such as eggshell, egg-white, and egg-yolk, was introduced to circumvent the rules by replacing the pellet sizes with the thickness of the catalytic layer of several hundreds of micrometres [23,24]. However, a significant volume of unused catalyst pellets exists, which reduces the volumetric productivities and leads to varying reaction fronts, as well as thermal and mass fronts within the reactor. As far as we know, the study on the influence of diffusion resistance on antibiotic pollutant purification by PMS-based AOPs is limited. Moral-Rodriguez et al. investigated the intraparticle diffusion of ronidazole and SMX during adsorption onto granular activated carbon (1.016 mm) from an aqueous solution. Their findings indicated that the overall adsorption rates of both antibiotics were primarily controlled by intra-particle diffusion [25]. This also necessitates the exploration of novel catalyst substrates to resolve persistent challenges associated with intraparticle diffusion at large particle sizes.

In this study, we fabricated the innovative micro-structured ceramic beads (MSCBs) with a significantly improved diffusion pathways to maximise the degradation efficiency of SMX, a representative reaction for other emerging organic pollutants in water. Unlike traditional beads, which consist of macro-pores formed by the random packing of micro- or meso-porous particles and have complex diffusion routes inside, these micro-structured ceramic beads dramatically boost the effective diffusivity. This enhancement is achieved by reducing diffusion restrictions from the random pore network through the creation of radial micro-channels, leading to a diffusion process that more closely mimics bulk
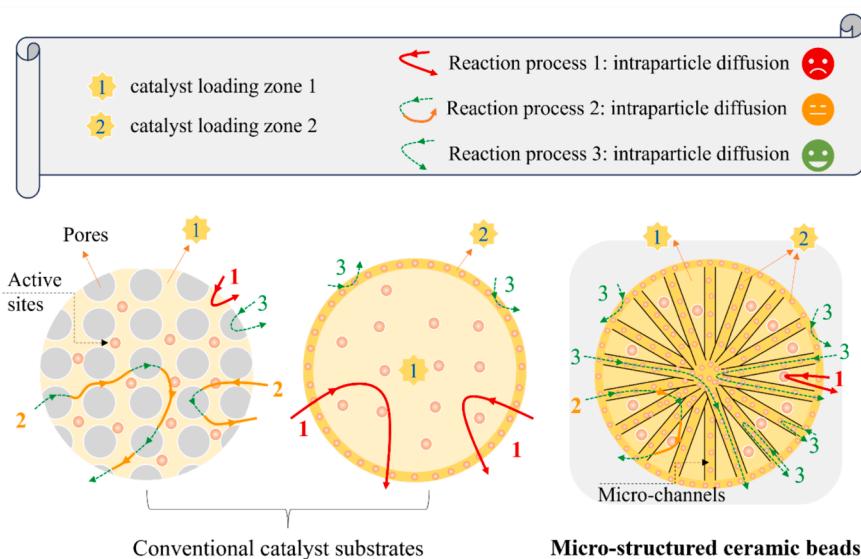

Fig. 1. Schematic diagram of diffusional transfer inside commercial catalyst substrates and novel micro-structured ceramic beads.

diffusion. This advancement will facilitate the potential upscaling of AOPs by better meeting with the industrial requirements for the catalytic materials. Herein, a transition metal catalyst, Co_3O_4, was impregnated in the MSCBs for the degradation of SMX in the PMS-activated AOPs reaction system under different reaction conditions (e.g., catalyst concentration, reaction temperature, and SMX concentration). The morphologies of the cross-sectional and surface of these ceramic beads were examined by SEM and EDS analysis, and other physicochemical properties were systematically characterised. Furthermore, the stability and reusability of the as-prepared 2Co/MSCBs were investigated. Finally, the active species involved in the 2Co/MSCB2|PMS reaction system were analysed through quenching experiment, and the catalytic mechanism of this reaction system was further proposed.

2. Materials and methods

2.1. Chemicals and materials

Alpha-alumina powder and Yttria Stabilized Zirconia (YSZ) grinding media were purchased from Inframat Advanced Materials (USA). Poly (methyl methacrylate) (PMMA), Oxone® (PMS, $KHSO_5 \cdot 0.5KHSO_4 \cdot 0.5K_2SO_4$), sulfamethoxazole (SMX), p-benzoquinone (p-BQ, ≥98 %), *tert*-butanol (tBA, ≥99.5 %), sodium azide (NaN$_3$, ≥99.5 %), and acetic acid (ReagentPlus®, ≥99 %) were all provided by Sigma-Aldrich. Cobalt nitrate hexahydrate (Co (NO$_3$)$_2$·6H$_2$O, 99 % pure)/methanol (HPLC grade, ≥99.8), polyethersulfone (PESf, Radel A-300), N-methyl-2-pyrrolidone (NMP, 99+%, ACS reagent) and ethyleneglycol 30-dipolyhydroxystearate (Arlacel P135) were provided by Fisher Scientific, Ameco Performance (USA), ACROS Organics and Uniqema (UK), respectively. All chemicals were used as received without any further purification. Milli-Q water (18.3 MΩ cm) was used during the whole experimental process.

2.2. Preparation of micro-structured ceramic beads (MSCBs)

Micro-structured Al_2O_3-based beads of 2–3 mm in diameter were fabricated for by a phase-inversion and sintering method, as shown in Fig. 2, inspired by the work in Li's group [26,27]. Specifically, prior to the addition of α-alumina powders (150 g), Arlacel P135 (1.05 g) was dissolved in NMP solvent (122.41 g), and the mixture was milled with 20 mm agate milling balls with an approximate alumina/agate weight ratio of 2 for 48 h. After the addition of PMMA, the suspension was continued for milling for another 48 h. The suspension was then transferred to a gas-tight vacuum degassing chamber (DP 27, Applied Vacuum Engineering) and degassed under vacuum for 3 h until no bubbles were visible at the surface, and then the suspension was transferred to a 100 mL stainless steel syringe fitted with polytetrafluoethylene O-rings and extruded at 0.1 mL/min into a water bath (a non-solvent for the polymer). The actual flow rate of the extrusion was controlled by a Chemyx Fusion 6000-X syringe pump, ensuring the uniformity of the prepared precursor ceramic beads. These precursor ceramic beads were kept in the water bath for 24 h to allow the completion of phase inversion.

Finally, the dried ceramic beads were sintered in stagnant air (furnace BRF 16/5, Elite) at 600 °C for 2 h and then 1450 °C for 4 h with a heating rate of 5 °C /min. The sintered micro-structured ceramic beads were named as MSCB1. Afterwards, the thin skin layer on the surface of MSCB1 was removed by blending them with coarse silica carbide (46 grit) in a volume ratio of 1:2 and place them in the Jarmill. The continuous rotation of SiC and MSCB1 in the Jarmill ensures the removal of skin layer due to wear and abrasion caused by the higher Moh's hardness of SiC (13) than α-Al$_2$O$_3$ (9). The resulting sample was denoted as MSCB2. For comparison, ceramic beads without radial microchannels (MSCB0) were prepared by the same method, wherein PMMA was substituted with PESf, and the quantity of NMP was augmented from 122.41 to 133.95 g.

It is worth noting that the formation of spherical ceramic beads is dependent on various operating parameters, e.g., suspension compositions, extrusion rates, nozzle dimensions, air gap and even the depth of the water bath. Detailed experiments and discussions are summarised in Text S1 in the supplementary information.

2.3. Preparation of Co-based catalytic ceramic beads (Co/MSCBs)

Cobalt oxide was loaded on the ceramic beads by the traditional incipient wetness impregnation (IWI) method, where a pre-determined
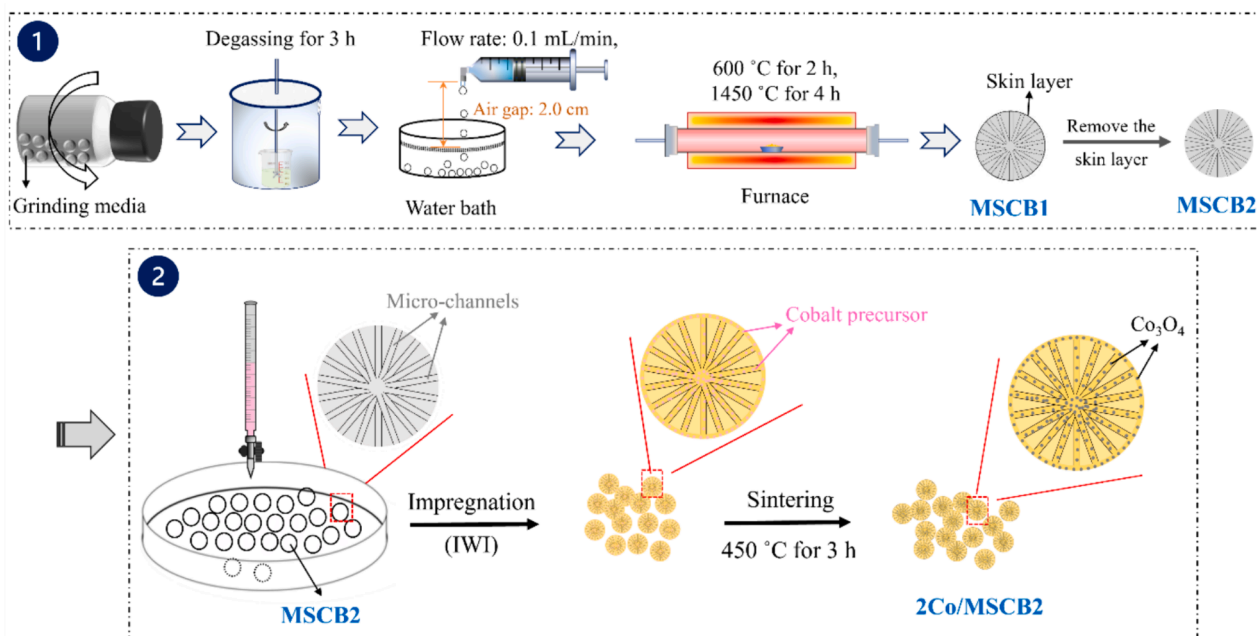

Fig. 2. Schematic illustration of the preparation of the micro-structured ceramic beads and the cobalt incorporation process, via phase inversion and incipient wetness impregnation method, respectively.

volume of cobalt nitrate hexahydrate aqueous solution was added onto the ceramic beads [28,29]. Then, the catalyst precursor was dried at 35 °C overnight before being calcined at 450 °C in stagnant air for 3 h at heating and cooling rates of 5 °C /min, as shown in Fig. 2. The as-prepared samples were denoted as *x*Co/MSCB*y*, where "*x*" refers to the weight percentage of Co_3O_4 to the ceramic beads, and "*y*" implies the specific ceramic beads (e.g., MSCB2 for the micro-structured ceramic beads without the skin layer).

2.4. Characterisation

Powder X-ray diffraction (XRD) spectra were recorded on an advanced X-ray diffractometer (Bruker D8, Germany) with Cu Kα radiation (λ = 1.5418 Å) in the range of 2θ = 5-80° at room temperature, operated at 40 kV and 40 mA. The chemical composition analyses were investigated on an X-ray photoelectron spectroscopy (XPS, Thermo Scientific K-Alpha Photoelectron spectrometer, USA) system equipped with an Al Kα source. All binding energies were calibrated using the contaminant carbon (C 1s = 284.8 eV) as a reference. The pore sizes and pore volumes of samples were obtained at −196 °C with liquid nitrogen on a Nova 4000 porosimeter, using the Brunauer–Emmett–Teller (BET) method and the Barrett, Joyner, and Halenda (BJH) method. Prior to the measurement, samples were gently ramped to 130 °C and degassed under vacuum for 5 h. The morphology and composition of ceramic beads were analysed by a scanning electron microscopy (SEM, JEOL JSM-IT200, operating at 5 kV and working distance of 10 mm) and energy-dispersive X-ray spectroscopy (EDS), respectively. Mercury intrusion porosimetry (Autopore IV 9500, Micromeritics) was used to investigate the pore structure of ceramic beads before and after removing the outer skin layer. The mercury intrusion data were collected under absolute pressure ranging from 0.10 to 60000.00 psia with an equilibration time of 10 s. The cobalt content in aqueous solutions was analysed by an ICP-OES apparatus (iCAP 7000 Series).

2.5. Activation of PMS in a batch catalytic degradation system

The catalytic performance of Co/MSCBs was evaluated for the degradation of SMX solutions in a PMS activated system. The experiments were carried out in a batch reactor in a water bath at 20 °C and connected with a mechanical overhead stirrer. Initially, a certain amount of catalyst was dispersed in 100 mL of SMX solution with a concentration of 20 mg/L with vigorously stirring at 150 rpm for 30 min to achieve the adsorption–desorption equilibrium. Afterwards, the catalytic reactions were triggered by adding PMS (0.31 mM) and continued for another 120 min. When the reaction was in process, 1 mL of aqueous solution was withdrawn by a syringe at fixed time intervals and filtered by a 0.2 μm PTFE syringe filter, and then immediately injected into a HPLC vial which was already injected with 0.5 mL methanol as a quenching agent. This is because that methanol has a high reactivity with both ·OH and SO_4^- ($k_{·OH}$ = 9.7 × 10^8 $M^{-1}s^{-1}$, $k_{SO4·-}$ = 3.2 × 10^6 $M^{-1}s^{-1}$) [30,31]. The concentrations of SMX solutions were analysed on an ultra-high performance liquid chromatography (UHPLC, Shimadzu Prominence, Japan) using a UV detector set at 270 nm of wavelength. A C^8 column (Restek Rapter, 2.7 μm, 100 × 2.1 mm, France) was used to differentiate the organics and the column oven temperature was set to 45 °C. Methanol and ultrapure water (pH of 3.5 adjusted by acetic acid) with a volume ratio of 9:1 was used as the mobile phase at a flowrate of 0.3 mL/min. The catalytic degradation kinetics of SMX followed the pseudo-first-order kinetic model and can be estimated using the following equation:

$$\ln(\frac{C}{C_0}) = -kt \qquad (2)$$

where k is the apparent reaction rate constant (min^{-1}), and C_0 and C are the initial SMX concentration (mg/L), and the SMX concentration at specific time intervals (mg/L), respectively [32].

3. Results and discussion

3.1. Characterisations of ceramic beads and Co-based MSCBs

The crystallographic structures of ceramic beads before and after cobalt impregnation were analysed by XRD. As shown in Fig. 3 (a), all diffraction peaks were well matched with the rhombohedral phase of Al_2O_3 referenced in JCPD file no. 88-0826 [33]. However, the characteristic peaks of Co_3O_4 were barely visible in three cobalt-based samples, which can be attributed to the low concentration and high dispersion of cobalt oxide [34]. This is supported by the XRD patterns of ceramic beads MSCB2 with a higher Co_3O_4 loading (Fig. 3 (b)), high-resolution XPS spectra of Co in the sample 2Co/MSCB2 (Fig. 3 (f)), the EDS mapping images (Fig. 6), alterations in colour of the cobalt oxide concentration from 0.5 wt% to 5 wt% (Fig. 10 (a)), and the ICP results (Fig. 10 (c)). It can be seen from Fig. 3 (b) that the main characteristic peak at 36.9°, indexed to the (3 1 1) plane of Co_3O_4 (JCPDS # 42-1467), appeared when the Co_3O_4 loading increased to above 5 w.t% (5Co/MSCB2) [35,36]. In fact, a small characteristic peak for (3 1 1) plane of Co_3O_4 could be found when zooming in the x-axis in the coordinate, as shown in the inset of Fig. 3 (a), further confirmed the existence of Co_3O_4.

Additionally, chemical compositions of the sample 2Co/MSCB2 were further investigated by XPS analysis, as shown in Fig. 3 (c-f). Fig. 3 (c) exhibited elemental compositions of 2Co/MSCB2 in the XPS survey spectra, which confirmed the presence of elements Al, O, C and Co. The C 1s spectrum belongs to the adventitious carbon originated from the carbon grid during the sampling process. In Fig. 3 (d), the main peak at 73.8 eV could be attributed to Al^{3+}, while the extremely weak peak at 75.3 eV resulted from the formation of small amounts of aluminium suboxide during the cobalt impregnation process [37,38]. The O 1s spectrum in Fig. 3 (e) could be divided into two components: the signal at 530.5 eV is characteristic peak of lattice oxygen species in Al-O bond of Al_2O_3, and 531.3 eV was related to the Al-O–H, suggesting that hydroxyl groups were attached on the surface of Al_2O_3 [39,40]. The existence of hydroxyl groups could be either attributed to residue water precursors during the process, or to the exposure of the catalysts to humid atmospheres prior to the XPS measurement [41]. As for the Co 2p spectra (Fig. 3(f)), two peaks at 780.0 eV and 795.0 eV corresponded to Co $2p_{3/2}$ and Co $2p_{1/2}$ of Co^{3+}, respectively, while two subpeaks at 781.6 eV and 797.1 eV were associated with Co $2p_{3/2}$ and Co $2p_{1/2}$ of Co^{2+}, respectively [42,43]. A spin energy interval of 15 eV refers to the mixed valence of Co_3O_4 [44]. Furthermore, two prominent shake-up satellite peaks (denoted as "Sat.") for Co^{2+} could also be observed at binding energy of 786.4 eV and 804.5 eV [45]. These findings further testified the successful incorporation of Co_3O_4, aligning with the XRD results.

Prior to conducting SEM analysis, ceramic beads were halved using a knife to expose their cross-sections, and the corresponding SEM images of both the cross-sectional and surface views can be observed in Fig. 4. Fig. 4 (a) and Fig. 4 (b) depict the sponge-like structure in both the cross-section and surface of MSCB0, while Fig. 4 (c) reveals a finger-like structure of MSCB1 in the cross-section with exposed microchannel sizes ranging from 150 to 1200 μm in length and 50 to 100 μm in width, depending on the cutting patterns. It is worth noting that the actual dimensions of microchannels are relatively uniform, as these structures developed in all directions inside the beads. Apparently, a dense sponge-like skin layer with a thickness of 70 μm on the cross-sectional edge of MSCB1 could be noticed, as corroborated by the surface view of MSCB1 depicted in Fig. 4 (d), which exhibits a similar sponge-like structure to that of MSCB0. However, it can be seen from Fig. 4 (e-h) that the dense skin layer disappeared in MSCB2, and some small open channels with diameters ranging from 1.97 to 15.54 μm (Fig. 4 (f) and Fig. 4 (i)) could be observed on the surface layer of the beads. This confirmed that the skin layer has been successfully removed, facilitating the transportation
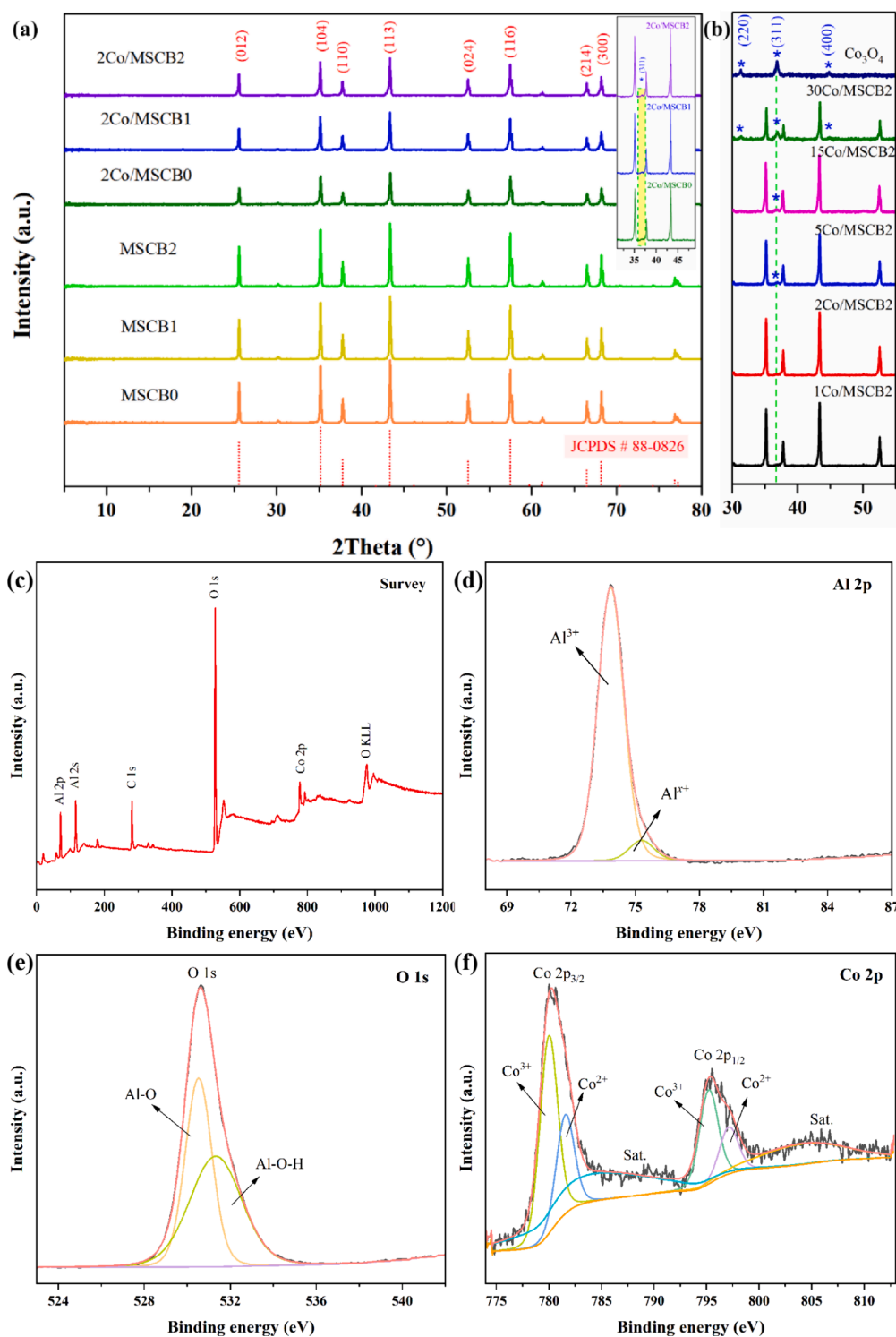
Fig. 3. XRD patterns of (a) three types of ceramic beads (MSCB0, MSCB1, MSCB2) before and after Co_3O_4 impregnation, and (b) ceramic beads MSCB2 with different Co_3O_4 loading. (c) XPS survey spectra and high-resolution XPS spectra of (d) Al (e) O, and (f) Co for the sample 2Co/MSCB2.

of reactants and products in catalytic reactions.

After incorporating with 2 wt% Co_3O_4, these samples were further analysed by SEM analysis and EDS mapping to investigate the formation and dispersion of cobalt oxide. Fig. 5 confirms that the introduction of Co_3O_4 did not change the pristine morphologies of ceramic beads. The EDS mapping of Al, O and Co elements on both the cross-sectional view (Fig. 6 (a)) and surface view (Fig. 6 (b)) of MSCB2 demonstrates the high stability of these MSCBs and the high dispersion of Co_3O_4. Noting that

the difficulty in identifying Co_3O_4 within the micro-channels of the cross-sectional view in Fig. 6 (a) arises from the fact that the depth of pores falls below the detectable limit of the equipment. Furthermore, the EDS mapping of MSCB0 (Fig. S5 (a)) and MSCB1 (Fig. S5 (b-c)) demonstrated comparable extensive cobalt dispersion.

The textural characteristics of three types of ceramic beads before and after cobalt impregnation were depicted by the nitrogen physisorption experiments, as shown in Table S1. It could be found that all
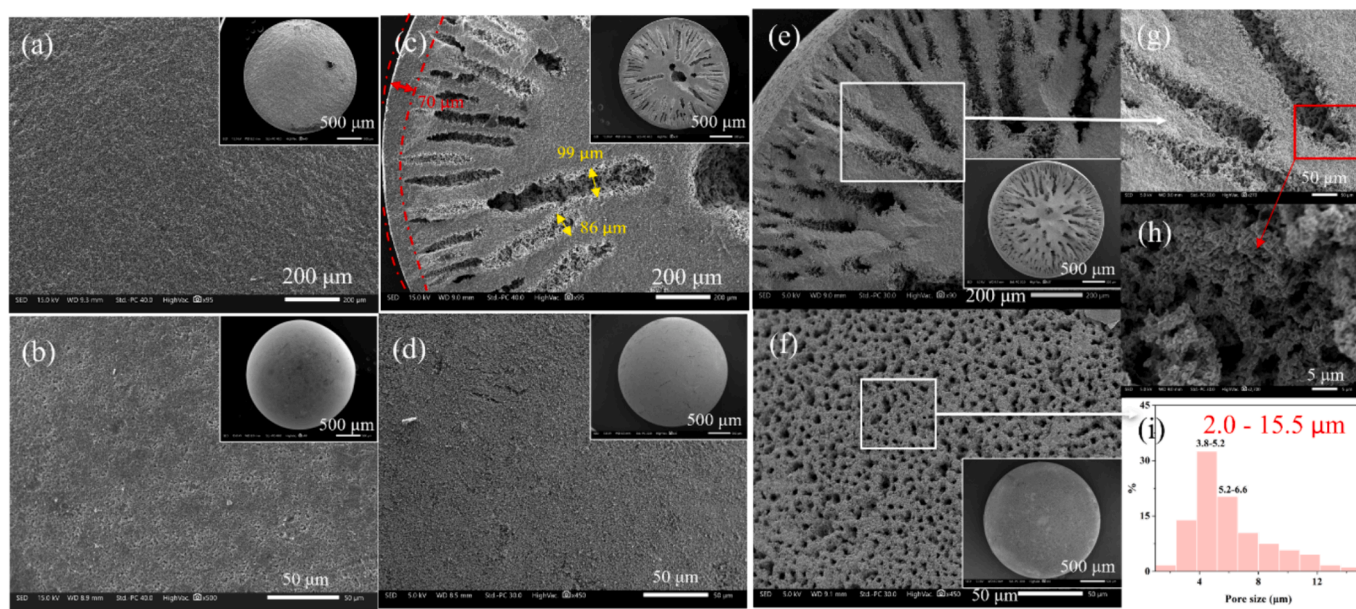
Fig. 4. SEM images of (a) the cross-sectional view and (b) the surface view of MSCB0, (c) the cross-sectional view and (d) the surface view of MSCB1, (e, g, h) the cross-sectional view, (f) the surface view, and (i) the size distribution of open channels on the surface of MSCB2, along with their corresponding whole views (inset).
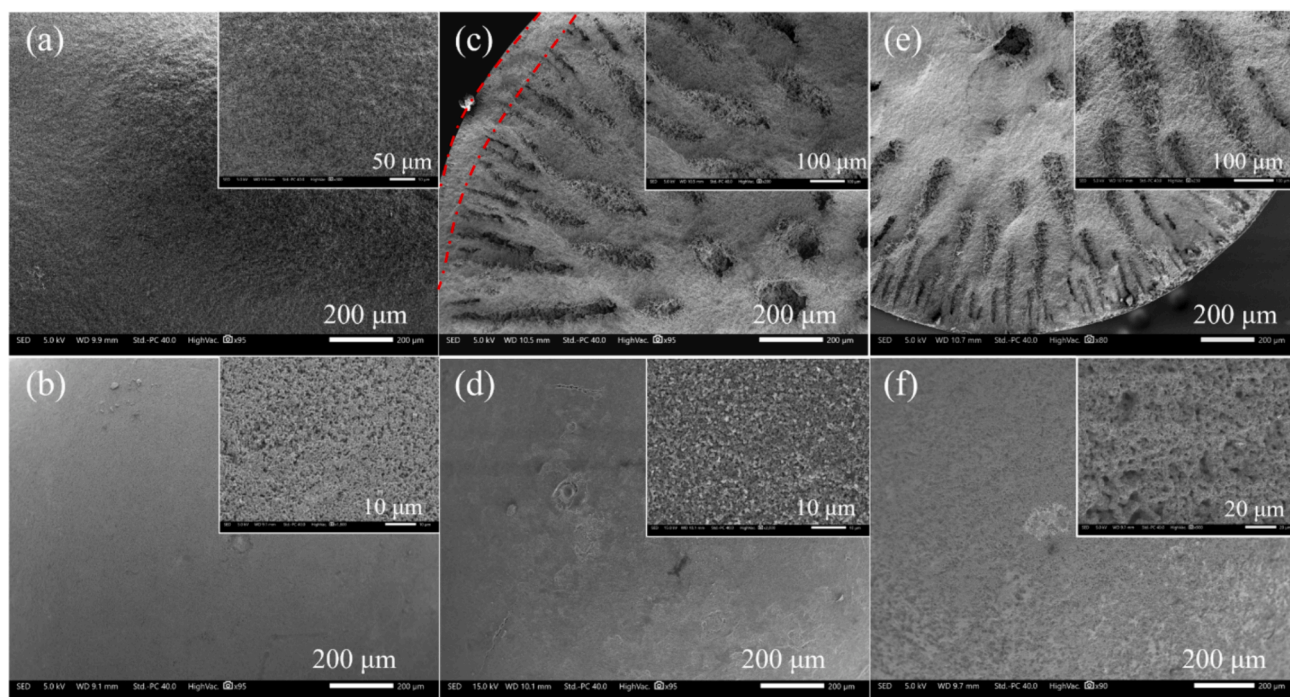

Fig. 5. SEM images of (a) the cross-sectional view and (b) the surface view of 2Co/MSCB0, (c) the cross-sectional view and (d) the surface view of 2Co/MSCB1, (e) the cross-sectional view and (f) the surface view of 2Co/MSCB2, along with their corresponding whole views (inset).

samples have small surface area owing to the intrinsic properties of α-Al$_2$O$_3$ and there were no significant differences among them in terms of surface area, total pore volume and pore diameters.

The limitations of the BET method in assessing anisotropic pore structures necessitated the use of mercury intrusion porosimetry (MIP). As depicted in Fig. 7, the distribution curve for these ceramic beads reveals different pore structures. MSCB1 has smaller pores with an average diameter (D_p) of 387.5 nm, while MSCB2 has significantly larger pores with a broader size distribution (D_p ranging from 5000 to 300,000 nm). The MIP measurement mechanism, which requires a higher pressure for mercury to infiltrate smaller pores, suggests that

387.5 nm represents the average pore size of the skin layer on MSCB1′s outer surface (refer to Fig. S6 (c) and the inset (1) in Fig. 7). The peak area of the distribution curve thus represents the pore volume of both the sponge-like structure and the radial micro-channels. Upon removal of the skin layer, mercury can directly access the micro-channels at a substantially lower pressure. This results in the detection of larger pores in MSCB2 (the insect (2) in Fig. 7). Increasing the pressure further allows mercury to infiltrate the remaining sponge-like pores within the beads. These observations are consistent with the SEM results presented in Fig. 4. For additional details on MIP measurements for other MSCBs samples with different specifics, refer to Figure S6. Additionally, the
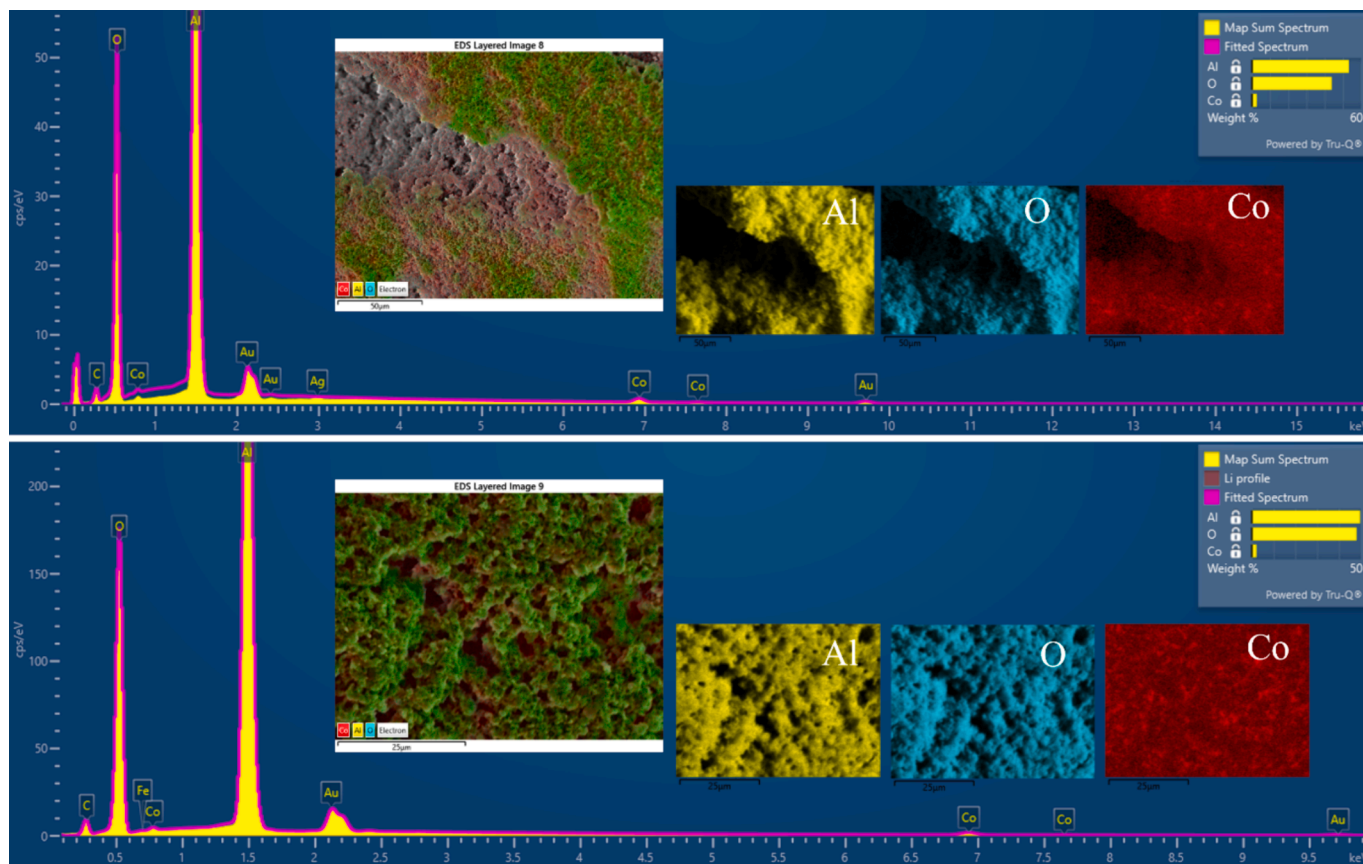
Fig. 6. EDS mapping results of Al, O and Co elements for the cross-section of (a) 2Co/MSCB1 and (b) 2Co/MSCB2.
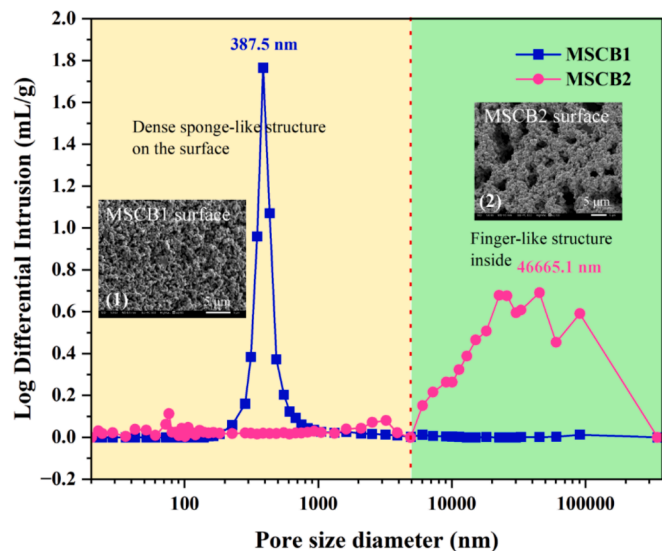

Fig. 7. Pore size distribution of micro-structured ceramic beads with dense sponge-like structures (MSCB1) and exposed open channels (MSCB2) on the surface layer.

porosity and pore volume data of MSCB1 and MSCB2 exhibit minimal changes. This can be attributed to the thin skin layer, which constitutes less than 5 % of the bead radius.

3.2. Catalytic degradation of SMX

In the liquid–solid reaction system, intraparticle diffusion is typically taking place, especially for catalyst particles with a diameter larger than 0.20–0.25 mm [46]. However, the creation of micro-channels within catalyst substrates can address this problem by enabling the radial micro-channels to serve as a "highway", thereby facilitating the transport of the reactants and products. Herein, the influence of the microstructures of catalyst substrates was investigated by the degradation of SMX under different reaction conditions, such as the reaction temperatures and SMX concentrations, as shown in Fig. 8 and Fig. 9. Before finalising the PMS dosage for three types of samples, the effect of various PMS concentrations has been investigated (Fig. S7), with 0.31 mM exhibiting the most suitable catalytic performance (28.1 %). This is comparable to the research with a similar PMS dosage [47,48]. Fig. 8 (a) displays the degradation of 20 mg/L SMX at 20 °C using the three ceramic beads. It is evident that the self-degradation of SMX and its purification using 2Co/MSCB2 only were negligible (0.1 %), and there was limited difference among these samples under this reaction condition, with 2Co/MSCB2 (70.5 %) slightly surpassing others. This is consistent with the results of the corresponding reaction kinetics (Fig. 8 (b)) and rate constants (Fig. 8 (c)). It is worth noting that at the beginning stage (5 min), the reaction rate constant k_{app} for 2Co/MSCB0 (0.04572 min^{-1}) is the lowest compared to 2Co/MSCB1 (0.05279 min^{-1}) and 2Co/MSCB2 (0.05285 min^{-1}). This is mainly attributed to the greater intra-particle diffusion resistance caused by the isotropic structure of 2Co/MSCB0. As the reaction continued, this disparity gradually diminished because the concentration gradient of the contaminants between external and internal surfaces of the catalyst support decreased. Additionally, the diffusion coefficient in liquid phase (10^{-10}–10^{-9} m^2/s) is very slow and is almost always overshadowed by convection.

Nevertheless, as the SMX concentration increased to 40 mg/L (Fig. 8 (d)), the degradation efficiency saw an enhancement from 49.6 % with 2Co/MSCB0 to 59.1 % with 2Co/MSCB2, indicating that the specific
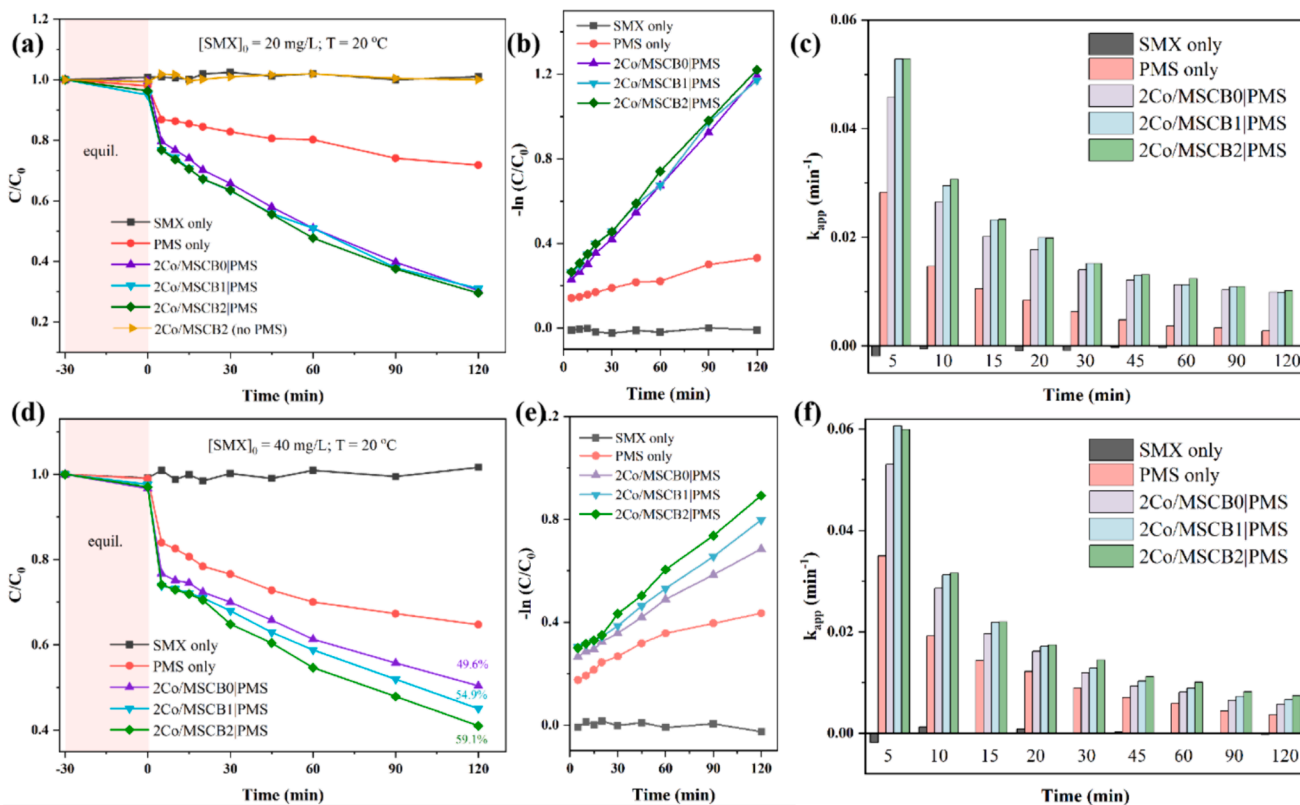
Fig. 8. Degradation of different SMX concentrations at 20 °C, their reaction kinetics, and the corresponding rate constants: (a, b, c) $[SMX]_0 = 20$ mg/L; (d, e, f) $[SMX]_0 = 40$ mg/L. Reaction Conditions: $[PMS]_0 = 0.31$ mM, $T = 20$ °C, $[catalyst]_0 = 0.2$ g/L, r = 150 rpm.
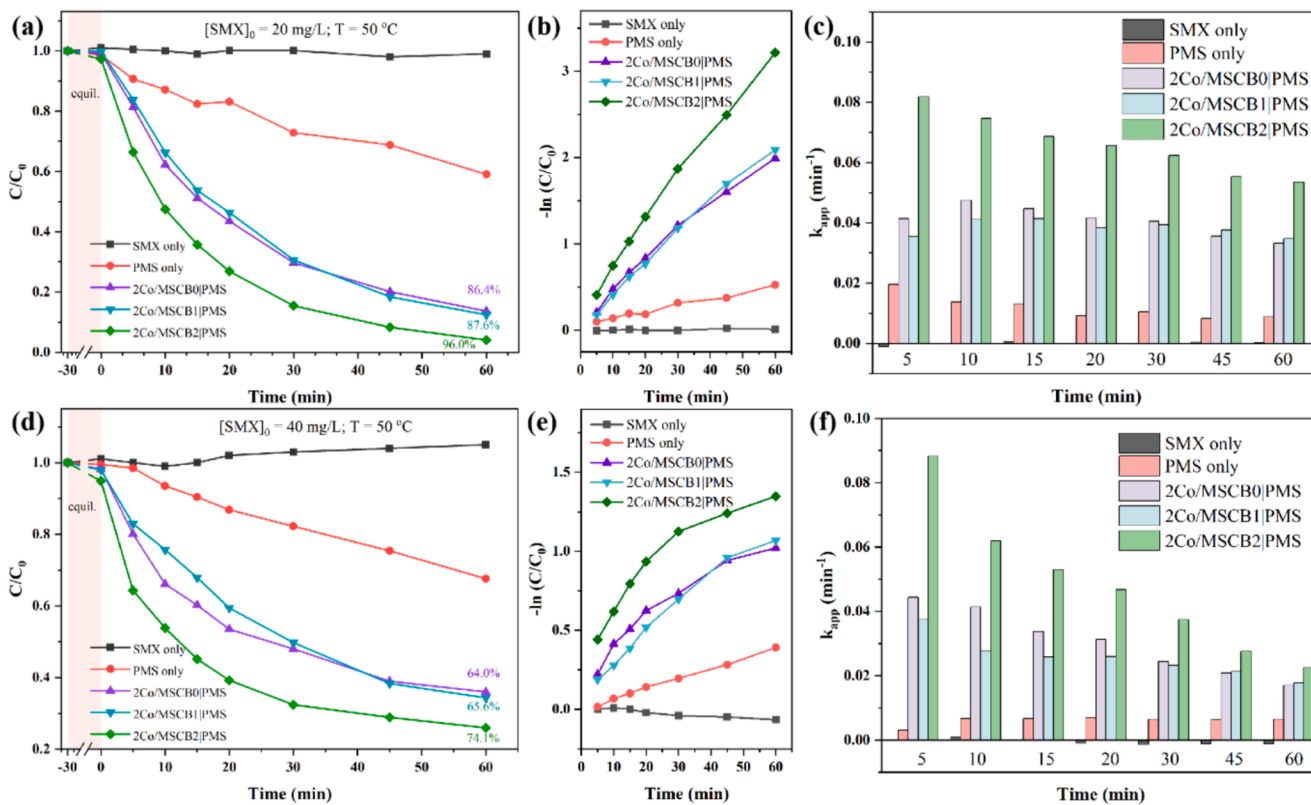

Fig. 9. Degradation of different SMX concentrations at 50 °C, their reaction kinetics, and the corresponding rate constants: (a, b, c) $[SMX]_0 = 20$ mg/L; (d, e, f) $[SMX]_0 = 40$ mg/L. Reaction Conditions: $[PMS]_0 = 0.31$ mM, $T = 50$ °C, $[catalyst]_0 = 0.2$ g/L, r = 150 rpm.

micro-channels within the ceramic beads promotes the transportation of reactants and products. Moreover, the exposed open channels on the surface layer of MSCB2 contributed to a reduction in diffusion resistance compared to the one with a thin dense skin on the surface layer, i.e., 2Co/MSCB1 (54.9 %). Likewise, Fig. 8 (f) indicates that the rate constants of 2Co/MSCB2 throughout the entire process were higher than those of 2Co/MSCB0, with the k_{app} value of 2Co/MSCB2 being 1.32 times that of 2Co/MSCB0. Further increasing the SMX concentration to 50 mg/L displayed a comparable scenario, as shown in Fig. S8 (a-b).

As known, reaction temperature is another key parameter for affecting the intra-particle diffusion as a higher temperature usually results in a faster movement of molecules. Apparently, Fig. 9 (a) revealed that 2Co/MSCB2 (96.0 %) performed the best catalytic performance within 60 min, in comparison to 2Co/MSCB0 (86.4 %) and 2Co/MSCB1 (87.6 %) when the reaction temperature increased from 20 °C to 50 °C for the degradation of SMX under the same reaction conditions. All catalysts showed increased catalytic activity as the activation energy for diffusion is lower at a higher temperature, according to Arrhenius equation [49].

$$D = D_0 \exp\left(\frac{-E_A}{RT}\right) \tag{3}$$

where D denotes the diffusion coefficient (in m²/s); D_0 is the maximal diffusion coefficient (in m²/s); E_A is the activation energy for diffusion

(in J/mol); R ≈ 8.31446 J/(mol·K) is the universal gas constant and T is the thermodynamic temperature (in K). The degradation efficiency of 2Co/MSCB0 and 2Co/MSCB1 is similar, which can be attributed to the thin skin layer (~70 μm) on the surface of the beads. Under this reaction condition, the rate constant of 2Co/MSCB2 is 1.62 times and 1.54 times of those of 2Co/MSCB0 and 2Co/MSCB1, respectively (Fig. 9 (c)). Similarly, the degradation patterns of 2Co/MSCB2 followed a similar trend with the elevation of SMX concentrations to 40 mg/L (Fig. 9 (d, e, f) and 50 mg/L (Fig. S8 (c, d) at 50 °C. Overall, the experimental advantages of this novel micro-structured catalyst substrate were investigated and verified by the PMS-activated AOPs reaction system.

Arrhenius law was applied to investigate the activation energy of 2Co/MSCB2 in the reaction system at three SMX concentrations.

$$k = Ae^{-\frac{E_A}{RT}} \tag{4}$$

where A denotes the pre-exponential factors. The reaction activation energies (E_A) were calculated via linear fitting of $\ln k$ versus $1/T$ and were determined to be 38.52 kJ/mol, 21.09 kJ/mol, and 14.20 kJ/mol for SMX concentrations of 20 mg/L, 40 mg/L, and 50 mg/L, respectively. These results demonstrate that the reaction between SMX solutions and 2Co/MSCB2 occurs more easily as SMX concentration rises. Given that the E_A values for SMX were higher than that of diffusion-controlled reactions (10–13 kJ/mol) [50], it can be concluded that the degradation process is dominated by the chemical reaction rate at the solid–liquid
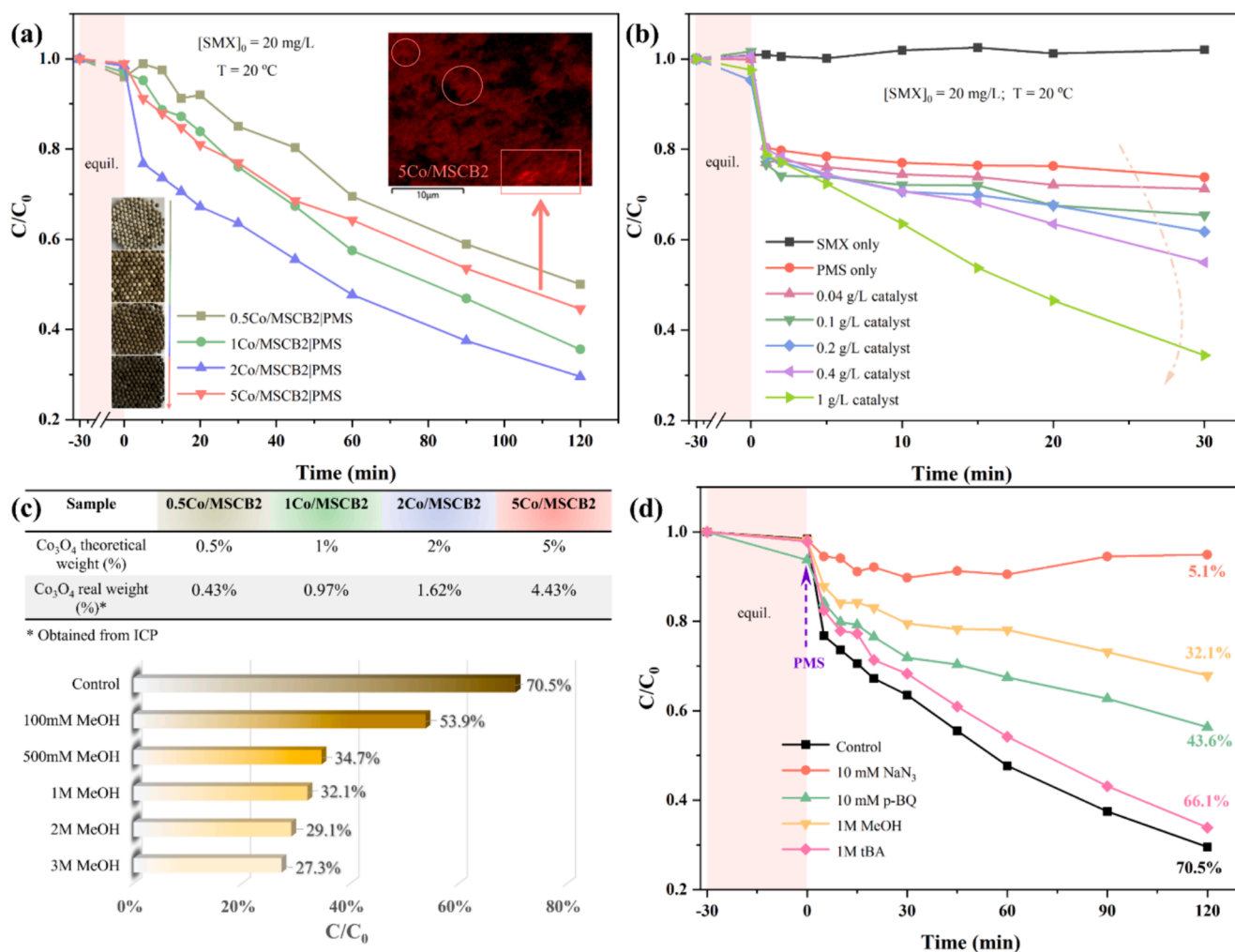

Fig. 10. Degradation profiles of SMX with different (a) Co₃O₄ loading ([catalyst]₀ = 0.2 g/L) and (b) catalyst concentration (catalyst: 2Co/MSCB2). (c) Co₃O₄ theoretical content and real content obtained by ICP method, and quenching effect on SMX degradation efficiency under different MeOH addition. (d) Effect of quenching agents on SMX degradation (catalyst: 2Co/MSCB2). Reaction Conditions: [PMS]₀ = 0.31 mM, [SMX]₀ = 20 mg/L, T = 20 °C.

interface. However, E_A for 50 mg/L SMX mineralization was nearly that of a diffusion-controlled reaction. This implies that increasing the SMX concentration further would lead to a diffusion-limited reaction, thereby enabling the structural advantages of this catalyst substrate more apparent. This will be explored in our future work.

In addition, the effect of Co_3O_4 loading and catalyst concentrations on SMX removal in Co/MSCBs|PMS system was further explored. As shown in Fig. 10 (a), the SMX removal rate rose as the Co_3O_4 loading increased from 0.5 wt% to 2 wt%, which could be attributed to the increased of Co_3O_4 addition, resulting in more active sites for PMS activation. This, in turn, generated more accessible ractive radicals ($SO_4^{\cdot-}$, $^{\cdot}O_2^-$, and $^{\cdot}OH$) for the reaction. However, further increasing it to 5 wt% led to a decline in SMX degradation efficiency, which could be attributed to the agglomoration of cobalt oxide, as supported by the SEM results in Fig. S4 (h-i) and EDS mapping result of Co in the insert of Fig. 10 (a). Herein, the brighter colour highlighted in the insert of Fig. 10 (a) mirror the backscattered electron detector-compositional (BED-C) images depicted in Fig. S4 (h-i), although conducting EDS mapping for micro-channels in the cross-section at high magnifications proved to be challenging due to the depth of these finger-like structures. It is worth noting that the colour of these beads changed from grey to dark as more cobalt oxide was loaded on them. The real Co_3O_4 content of all samples was investigated by ICP and is predented in Fig. 10 (c). The disparity between the expected weight and the real weight is minimal. Besides, Fig. 10 (b) shows that the SMX removal increased from 28.7 % to 65.6 % within 30 min with the catalyst dosage increase from 0.04 g/L to 1 g/L, thanks to more active sites. The leaching of cobalt ions in this reaction system was acceptable, as all catalytic systems showed cobalt leaching levels below 0.40 ppm, which aligns with the published work [51].

3.3. Possible catalytic reaction pathways and mechanism

In order to determine the main reactive species and their contributions to the 2Co/MSCB2|PMS system for SMX degradation, radical quenching experiments were carried out. Herin, certain amounts of NaN$_3$, p-benzoquinone (p-BQ), methanol (MeOH) and *tert*-butanol (tBA) were introduced into the 2Co/MSCB2|PMS system for the degradation of SMX, as shown in Fig. 10 (d). As known, NaN$_3$, p-BQ, and tBA could be

acted as the scavenger for $^1O_2$, $^{\cdot}O_2^-$, and $^{\cdot}OH$, respectively, while MeOH is commonly used as a quencher of $SO_4^{\cdot-}$ and $^{\cdot}OH$ [52,53]. When NaN$_3$ was introduced in the system, the SMX removal efficiency was significantly suppressed from 70.5 % to 5.1 %. Recent research by Wang's group revealed that NaN$_3$ could directly interact with PMS and affect the removal efficiency of target contaminants [54]. It is also reported that another popular $^1O_2$ quencher, furfuryl (FFA), could react with $^1O_2$ and $^{\cdot}OH$, and might also consume $SO_4^{\cdot-}$ during quenching tests [34]. Therefore, the depressed SMX degradation efficiency shown in Fig. 10 (d) may not directly indicate that $^1O_2$ plays a dominant role in the reaction system. Subsequent research will further examine the contribution of $^1O_2$ in the 2Co/MSCB2|PMS system. In contrast, the introduction of p-BQ and tBA caused a suppression of 26.9 % and 4.4 % for the degradation of SMX, demonstrating the partial contribution of $^{\cdot}O_2^-$ and the negligible effect of $^{\cdot}OH$, respectively. However, when MeOH was added, the degradation efficiency declined to 32.1 %, leading to a 38.4 % suppression of $SO_4^{\cdot-}$ and $^{\cdot}OH$, ultimately resulting in a 34.0 % reduction in $SO_4^{\cdot-}$ alone. Furthermore, as the methanol concentration rose from 100 mM to 500 mM, the inhibitory effect gradually intensified (Fig. 10 (c)). Continuing to increase it to 1 M, 2 M and 3 M led to limited alteration, with 27.3 % degradation still occurring during the reaction. This indicated that the 2Co/MSCB2|PMS reaction system may follow radical and non-radical pathways.

In summary, due to the co-existence of radical pathway ($SO_4^{\cdot-}$, $^{\cdot}O_2^-$, and $^{\cdot}OH$) and non-radical pathway ($^1O_2$) in the 2Co/MSCB2|PMS system, a possible catalytic mechanism for the efficient degradation of SMX in the 2Co/MSCB2|PMS system was proposed in Fig. 11. On the one hand, Co^{2+} on the surface of 2Co/MSCB2 could successfully be activated to generate $SO_4^{\cdot-}$, accompanying the formation of Co^{3+} (Eq. (4)). Simultaneously, the generated Co^{3+} can convert to Co^{2+} by reacting with HSO_5^-, resulting in the redox cycle of Co^{2+}/Co^{3+} and the formation of $SO_5^{\cdot-}$ (Eq. (5)). As reaction proceeded, the generated $SO_4^{\cdot-}$ was partially transferred to $^{\cdot}OH$ (Eq. (6)), but it played a negligible role (4.4 %) in this reaction system. At the same time, the produced $SO_5^{\cdot-}$ could be transformed to $SO_4^{\cdot-}$ (Eq. (7)). Moreover, some PMS reacted with $^{\cdot}OH$ to form $HO_2^{\cdot}$, and $HO_2^{\cdot}$ further self-decomposed to $^{\cdot}O_2^-$ (Eqs. (8)–(9)). In the non-radical pathway, $^1O_2$ can be produced by the consumption of $^{\cdot}O_2^-$ and $^{\cdot}OH$ (Eq. (10)). As per the synergistic interaction between radicals
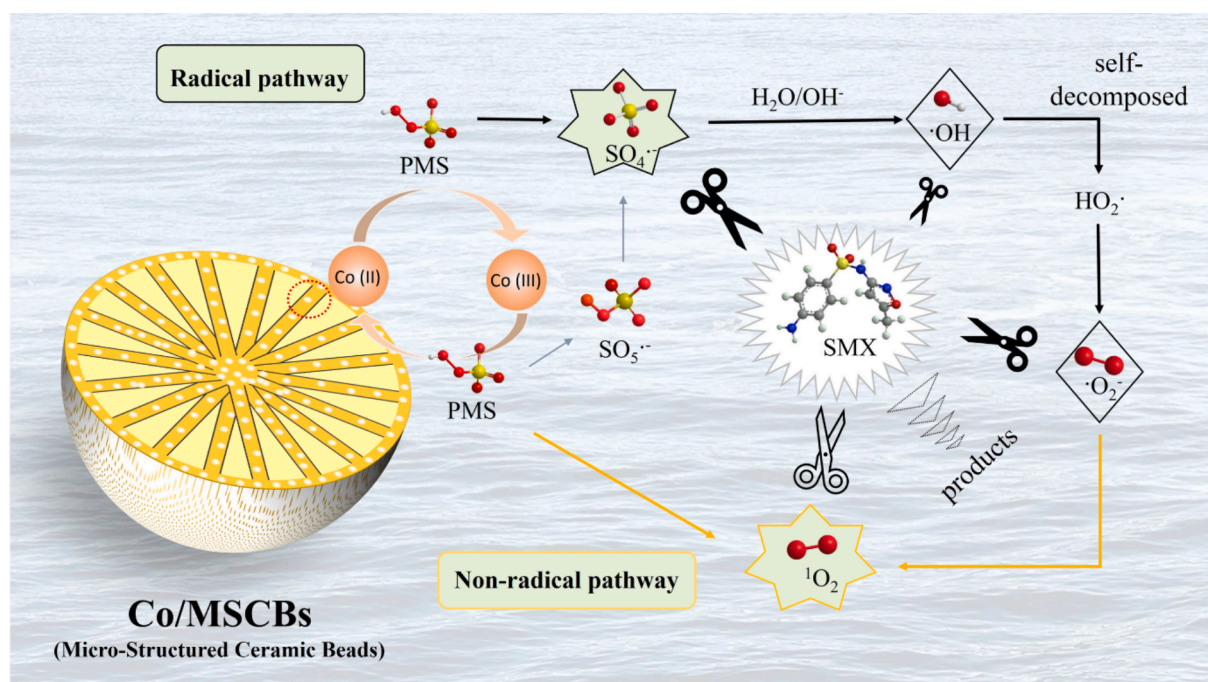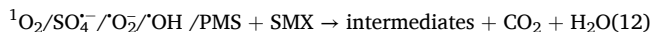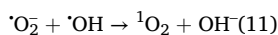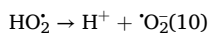

Fig. 11. A proposed mechanism for catalytic oxidation of SMX by 2Co/MSCB2|PMS system.

and non-radicals, the rapid regeneration of Co (II) was achieved, greatly enhanced the catalytic performance for PMS activation and SMX decomposition (Eq. (11)).

$$Co\ (II) + HSO_5^- \rightarrow Co\ (III) + SO_4^{\cdot -} + OH^- \quad (5)$$

$$Co\ (III) + HSO_5^- \rightarrow Co\ (II) + SO_5^{\cdot -} + H^+ \quad (6)$$

$$SO_4^{\cdot -} + OH^- \rightarrow {}^{\cdot}OH + SO_4^{2-} \quad (7)$$

$$SO_5^{\cdot -} + 2H_2O \rightarrow SO_4^{\cdot -} + {}^{\cdot}OH \quad (8)$$

$$HSO_5^- + {}^{\cdot}OH \rightarrow HO_2^{\cdot} \quad (9)$$

$$HO_2^{\cdot} \rightarrow H^+ + {}^{\cdot}O_2^- \quad (10)$$

$${}^{\cdot}O_2^- + {}^{\cdot}OH \rightarrow {}^1O_2 + OH^- \quad (11)$$
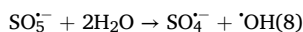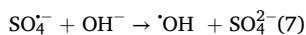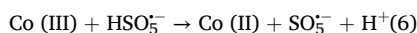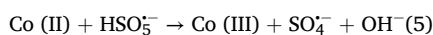
$${}^1O_2/SO_4^{\cdot -}/{}^{\cdot}O_2^-/{}^{\cdot}OH\ /PMS + SMX \rightarrow intermediates + CO_2 + H_2O \quad (12)$$
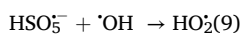
3.4. Reusability and stability of 2Co/MSCB2

Reusability is crucial for commercial and practical applications of catalysts. Fig. 12 shows the cyclic experimental results of the 2Co/MSCB2 for the SMX degradation with different regeneration methods under the same reaction conditions. As shown in Fig. 12 (a), when the catalysts were separated from the liquid phase and washed with DI water only, the SMX degradation decreased from 70.5 % to 63.5 %, 53.3 %, 46.7 % and 40.5 % within 120 min in the 2nd, 3rd, 4th, 5th run, respectively. This might be attributed to the adsorption of organic pollutants on the surface of catalysts, which reduced the amounts of exposed active sites, preventing the degradation of target organic pollutants, as evidenced by the SEM images (Fig. 13 (g)). Most importantly, the SMX removal efficiency recovered instantly after regenerating the catalysts by post-sintering at 450 °C for 1 h (6th cycle). More than that, 94.7 % of SMX was removed within 120 min in this cycle, surpassing the fresh one (70.5 %) by a considerable margin. The regenerated catalysts were capable to achieve a similar removal efficiency (69.8 %) with a reaction time of 45 min. However, the SMX removal efficiency fell back to its original level (59 %) when the catalysts were continuously used for the subsequent cycle (7th). Likewise, this phenomenon recurred during the second (12th, 98.7 % SMX removal in 120 min, 68.5 % SMX removal in 30 min) and third regenerations (16th, 100 % SMX removal in 120 min, 70.9 % SMX removal in 20 min), underscoring its scientific rather than sporadic nature. To the best of our knowledge, this is the first time that used AOPs catalysts could demonstrate a much higher catalytic performance than the fresh one. Zhu et al. reported a novel MOF-derived CuO-Fe₃O₄@C catalyst for bisphenol A mineralization, and the reusability results exhibited a similar trend to this work before and after regeneration [55]. Initially, the BPA removal efficiency was 100 %, but it dropped to 41.5 % after three consecutive cycles. When the catalyst was regenerated by washing and post-sintering, its performance immediately returned to 94.3 % for the third cycle. This aligns with most
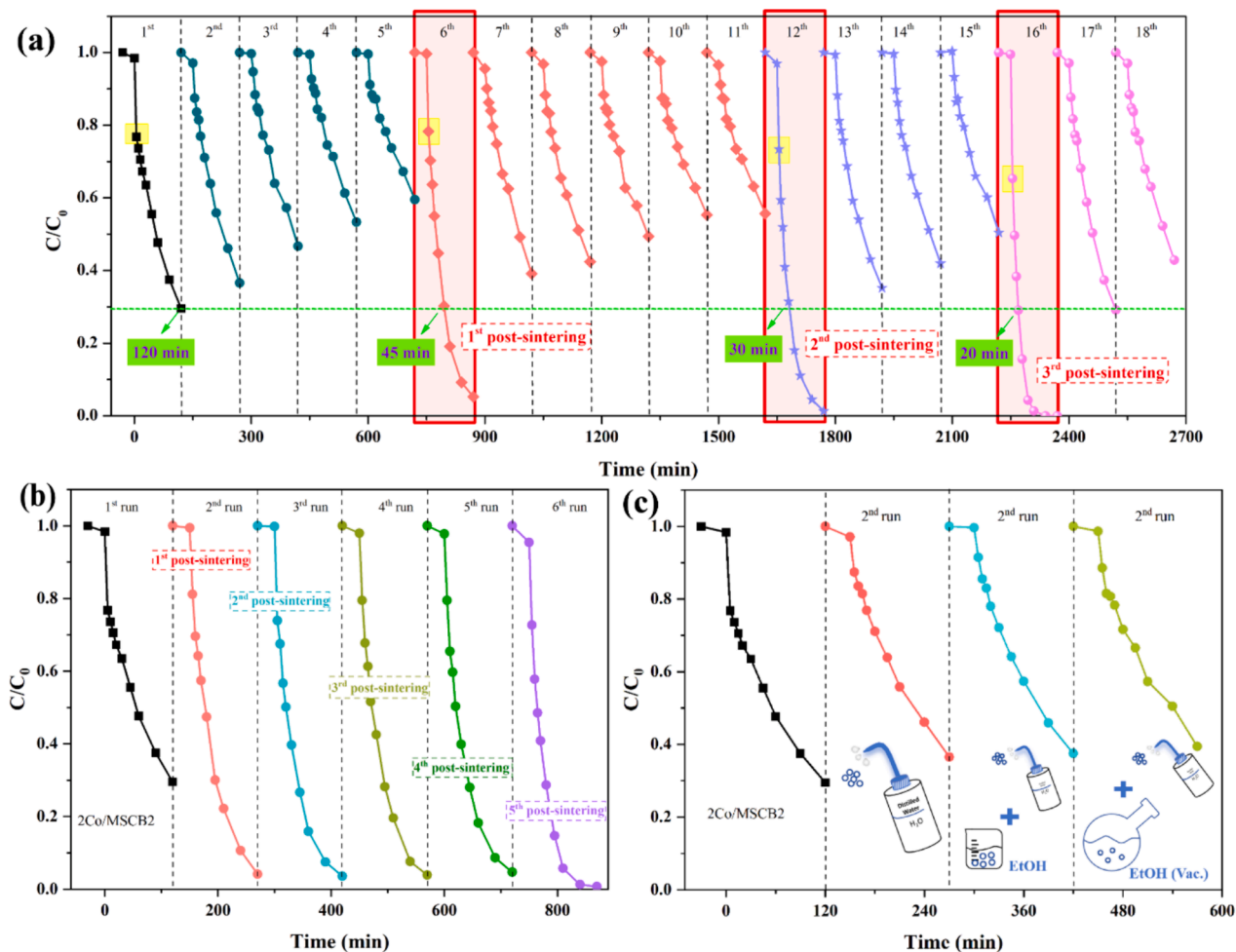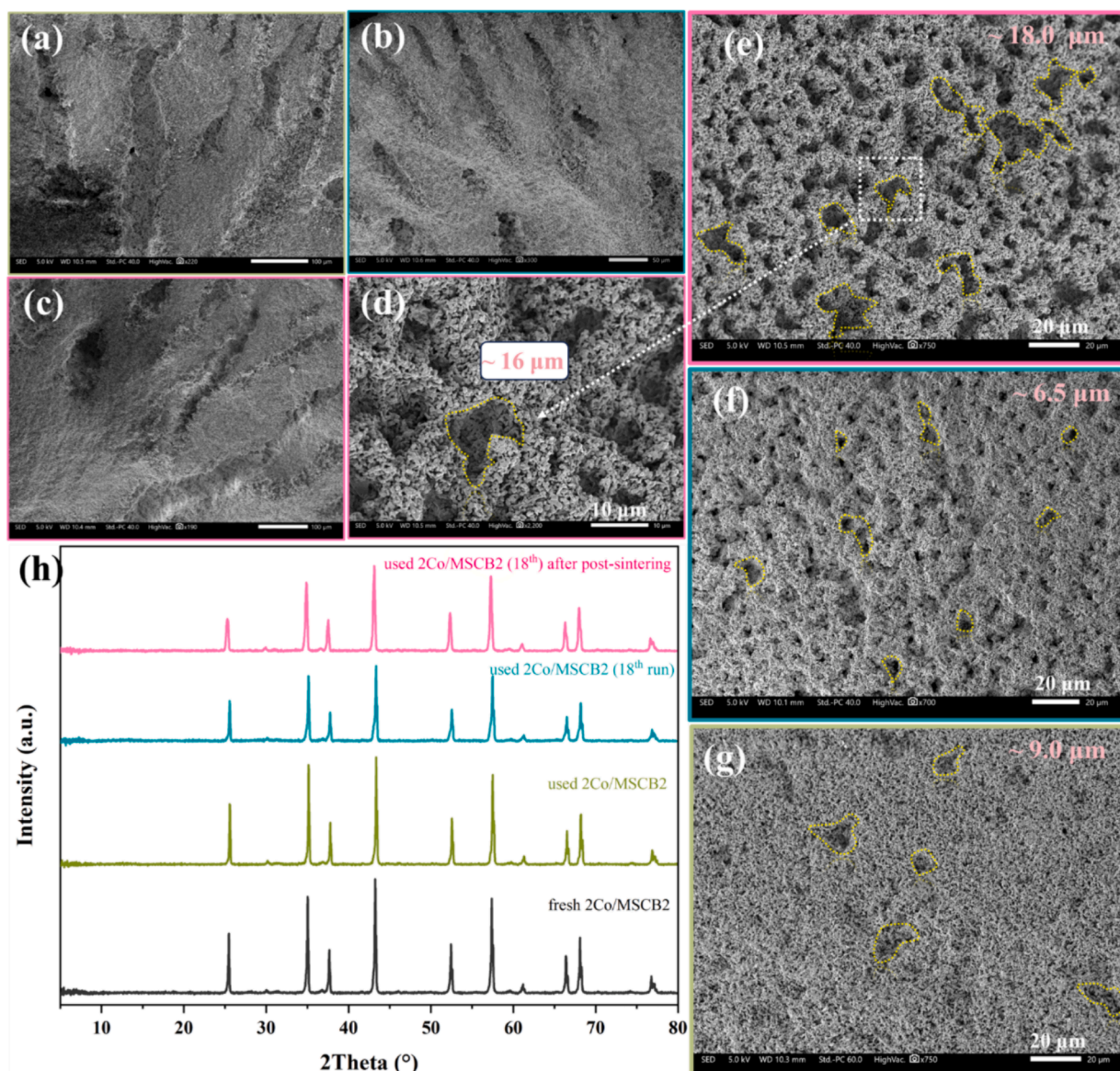

Fig. 12. Recycling and reuse of the 2Co/MSCB2 for (a) 18 successive cycles with cleaning by DI water only or regenerating by sintering at 450 °C for 1 h, (b) 6 successive cycles with regenerating by post-sintering at 450 °C for 1 h, and (c) two cycles with cleaning by different approaches. Reaction Conditions: [PMS]$_0$ = 0.31 mM, [catalyst]$_0$ = 0.2 g/L, [SMX]$_0$ = 20 mg/L, T = 20 °C.

Fig. 13. SEM images of cross-sectional view of 2Co/MSCB2 after recycled for (a) twice, (b) 18th, and (c) post sintering treatment after 18th cycles; SEM images of surface views of 2Co/MSCB2 after recycled for (g) twice, (f) 18th, and (d, e) post sintering treatment after 18th cycles; (h) XRD patterns of 2Co/MSCB2 before and after used.

previous research, where the reactivity and stability of catalysts technically exhibited a downward trend in the mineralization of antibiotic pollutants, although some studies demonstrated that catalysts retained high efficiencies comparable to the initial test over a few cycles [1,3,56]. These findings are still insufficient to verify their high cycling potential because of the continuous depletion of exposed active sites and the intrinsic properties of the catalyst powders. However, in this work, the unique catalyst substrate could facilitate the sustained exposure of accessible cobalt sites and reduce the intraparticle diffusion resistance over the long term. The major reason responsible for this was likely related to the larger and increased number of exposed open channels on the surface of the beads after post-sintering, as shown in Fig. 13 (e). The interesting findings provide a new insight into the preparation of catalysts and/or catalyst substrates in the academic and industrial applications.

In order to verify the impact of this regeneration method, another set of catalysts was employed for the cyclic experiments. The used catalysts were subjected to post-sintering at 450 °C for 1 h after each reaction, as illustrated in Fig. 12 (b). Obviously, the SMX degradation efficiency

enhanced gradually as the increase number of cycles, with SMX removal of 70.4 %, 95.8 %, 96.4 %, 96.1 %, 99.0 %, and 99.3 % for the 1st, 2nd, 3rd, 4th, 5th, and 6th cycle. This implies that post-sintering is a practical and efficient strategy for regenerating the used catalysts, thereby sustaining a notably improved degradation efficiency during continuous utilisations. Finally, Fig. 12 (c) demonstrated that apart from regenerating catalysts through post-sintering, there was minimal distinction among alternative approaches (i.e., cleaning with DI water three times, rinsing with DI water three times and ethanol three times, washing with DI water three times followed by washing with ethanol under vacuum in the round-bottom flask three times).

Fig. 13 depicts the XRD patterns and SEM images of fresh and used 2Co/MSCB2 samples. As shown in Fig. 13 (h), no obvious changes of XRD diffraction patterns could be observed among samples before and after use for once, 18 times, and 18 times after being regenerated by post-sintering. This revealed that the catalyst and catalyst substrate had excellent stability, which is accord with the cyclic experimental results in Fig. 12 (a). Additionally, with regard to the SEM morphologies among three samples after used, it is clear that although the cross-sectional view

of these beads (Fig. 13 (a-c)) did not undergo significant alterations, the sizes and number of open channels on the surface layer of beads (Fig. 13 (e-g) boosted as the cyclic experiments increased. The increased openness of the surface could potentially be attributed to the removal of loosely packed alumina powders during thermal cycles. These powders were formed on the bead surface during the grinding processes and partially blocked some surface pores. Moreover, the post-sintering process facilitated the clearage of adsorbed reactants and products, which are difficult to be cleaned by DI water and/or methanol. This is in keeping with the previous findings in Fig. 12 (c). As indicated in Fig. 13 (g), most of the exposed open channels on the surface layer of used 2Co/MSCB2 have been adsorbed and blocked by the reactants and products, with only a small number of pores (approximately 9 μm in diameter) could be detected. However, when the catalyst was used for 18 times, more detectable pores with smaller sizes (~6.5 μm) could be identified in Fig. 13 (f). This might be related to the exposure of inner layer of the bead surface after the active sites on the outer layer have been consumed during the reaction. Technically, when the phase inversion happens, the micro-channels commence near the surface region of the ceramic beads and progressively expand as they propagate, resulting in relative wider channels inside than that of the surface region [57]. Therefore, we can reasonably anticipate that with an increased number of cyclic experiments in this reaction system, there will be a further enhancement in catalytic performance owing to the more and larger exposed open channels. This aligns well with the efficacy of the MSCBs in reducing diffusional transfer resistance inside porous catalyst pellets. Furthermore, in contrast to the used 2Co/MSCB2 (18th run) with partial blockage of the open channels, further post-sintering treatment contributed to the complete clearance of adsorbed organic pollutants and products. This explains the larger pores, i.e., approximately 18 μm, in Fig. 13 (e) and Fig. 13 (d) and boosted catalytic performance in Fig. 12 (a). These findings represent a considerable breakthrough in the way of design catalyst substrates in catalytic reactions.

In contrast to conventional strategies, which focus on increasing the effective surface area of the nano catalysts or enhancing PMS activation through surface engineering of heterogeneous catalysts to expose more active sites and accessible surfaces, this work provided a new insight into improving the reactivity and stability of catalysts in PMS-activated cobalt-based AOPs systems. The large size of the 2Co/MSCB2 (3 mm in diameter), featuring distinctive radical micro-channels, can effectively address the long-standing challenge of balancing pressure drop and intra-particle diffusion in packed-bed reactors while also facilitating easy separation and recycling from the bulk fluid. Consequently, this study highlights significant advancements in catalyst technology research and demonstrates considerable potential for both academic and industrial applications.

4. Conclusion

In summary, novel micro-structured ceramic beads were successfully prepared for the first time by a simple phase-inversion and sintering-assisted method. Three different configurations of ceramic beads were analysed through various physiochemical techniques and employed for the catalytic oxidation of SMX in the PMS activated AOPs system. As expected, 2Co/MSCB2 exhibited the best degradation efficiency towards PMS activation as compared to 2Co/MSCB0 and 2Co/MSCB1, particularly when operating at higher SMX concentrations and higher reaction temperatures. The improved SMX removal efficiency could be attributed to the reduced diffusion resistance and abundant available active sites on the micro-channels inside the beads. Reaction parameters including catalyst dosage, SMX concentration, reaction temperatures validate the advantage of this specific catalyst substrate configuration. More importantly, 2Co/MSCB2 after used and regenerated exhibited a significantly higher catalytic performance (16th run, 70.83 % in 20 min) than the fresh one (70.47 % removal in 120 min), and this recurred when regenerating the catalysts by post-sintering at 450 °C for 1 h. This

could be ascribed to the more and larger exposed open channels on the surface layer of micro-structured ceramic beads, which further reduced the intraparticle diffusion resistance in the AOPs reactions. Furthermore, the radical quenching experiment was conducted, and the catalytic mechanism of the radical and non-radical pathways associated with SMX degradation were explored.

CRediT authorship contribution statement

Jiaojiao Zheng: Methodology, Formal analysis, Writing – original draft. **Hongqi Sun:** Validation, Data curation. **Kang Li:** Validation, Formal analysis, Writing – review & editing. **Zhentao Wu:** Conceptualization, Methodology, Formal analysis, Resources, Writing – review & editing, Supervision, Project administration, Funding acquisition.

Declaration of competing interest

The authors declare that they have no known competing financial interests or personal relationships that could have appeared to influence the work reported in this paper.

Data availability

Data will be made available on request.

Appendix A. Supplementary data

Supplementary data to this article can be found online at https://doi.org/10.1016/j.seppur.2024.129060.

References

[1] R. El Asmar, et al., Iron-based metal organic framework MIL-88-A for the degradation of naproxen in water through persulfate activation, Chem. Eng. J. 405 (2021).

[2] O. Mertah, et al., Peroxymonosulfate enhanced photodegradation of sulfamethoxazole with TiO2@CuCo2O4 catalysts under simulated solar light, J. Environ. Chem. Eng. 10 (5) (2022).

[3] R.A.K. Hirani, et al., Heterogeneous activation of persulfate by macroscopic nitrogen-doped graphene oxide cubes for the degradation of antibiotic contaminants in water, Sep. Purif. Technol. 319 (2023).

[4] L. Zhou, et al., Development of attapulgite based catalytic membrane for activation of peroxymonosulfate: A singlet oxygen-dominated catalytic oxidation process for sulfamethoxazole degradation, Sep. Purif. Technol. 312 (2023).

[5] A.H. Asif, et al., Graphitic carbon nitride engineered α-Fe2O3/rGO heterostructure for visible-light-driven photochemical oxidation of sulfamethoxazole, Chem. Eng. J. 451 (2023).

[6] A.H. Asif, et al., MIL-53(Fe) derived magnetic CuFe2O4/Fe2O3 composite for catalytic oxidation of sulfamethoxazole via peroxymonsulfate activation, Chem. Eng. J. 469 (2023).

[7] F. Zhang, et al., Co-Fe synergy in CoxFe1-xWO4: the new type peroxymonosulfate activator for sulfamethoxazole degradation, Chem. Eng. J. 461 (2023).

[8] M. Kohantorabi, G. Moussavi, S. Giannakis, A review of the innovations in metal- and carbon-based catalysts explored for heterogeneous peroxymonosulfate (PMS) activation, with focus on radical vs. non-radical degradation pathways of organic contaminants, Chem. Eng. J. (2021) 411.

[9] X. Duan, et al., Insights into perovskite-catalyzed peroxymonosulfate activation: maneuverable cobalt sites for promoted evolution of sulfate radicals, Appl. Catal. B 220 (2018) 626–634.

[10] R. Luo, et al., Convenient synthesis and engineering of ultrafine Co3O4-incorporated carbon composite: towards practical application of environmental remediation, J. Mater. Chem. A 6 (8) (2018) 3454–3461.

[11] H. Zhang, et al., Enhanced removal of lomefloxacin based on peroxymonosulfate activation by Co3O4/δ-FeOOH composite, Chem. Eng. J. 369 (2019) 834–844.

[12] Z. Cai, et al., Single-crystalline ultrathin Co3O4 nanosheets with massive vacancy defects for enhanced electrocatalysis, Adv. Energy Mater. 8 (3) (2017).

[13] Q. Yang, H. Choi, D.D. Dionysiou, Nanocrystalline cobalt oxide immobilized on titanium dioxide nanoparticles for the heterogeneous activation of peroxymonosulfate, Appl. Catal. B 74 (1–2) (2007) 170–178.

[14] Q. Yang, et al., Heterogeneous activation of peroxymonosulfate by supported cobalt catalysts for the degradation of 2,4-dichlorophenol in water: The effect of support, cobalt precursor, and UV radiation, Appl. Catal. B 77 (3–4) (2008) 300–307.

[15] M.-C. Li, et al., Enhanced degradation of 5-sulfosalicylic acid using peroxymonosulfate activated by ordered porous silica-confined Co3O4 prepared via a solvent-free confined space strategy, Sep. Purif. Technol. 249 (2020).

[16] J. Cheng, et al., Direct transformation of bulk cobalt foam into cobalt nanoparticles encapsulated in nitrogen-doped carbon nanotubes for peroxymonosulfate activation toward rhodamine B degradation, Sep. Purif. Technol. 277 (2021).

[17] W. Zhu, et al., ZIF-8-derived nitrogen-doped porous carbon supported CuFeO2 for sulfamethoxazole removal: Performances, degradation pathways and mechanisms, J. Environ. Chem. Eng. 11 (3) (2023).

[18] I.F. Macías-Quiroga, et al., Research trends on pillared interlayered clays (PILCs) used as catalysts in environmental and chemical processes: bibliometric analysis, Sci. World J. 2022 (2022) 5728678.

[19] A.-R. Kim, et al., Hydrogen production from ammonia decomposition over Ru-rich surface on La2O2CO3-Al2O3 catalyst beads, Catal. Today 411–412 (2023) 113867.

[20] M.-P. Zhu, et al., Deciphering the simultaneous removal of carbamazepine and metronidazole by monolithic Co2AlO4@Al2O3 activated peroxymonosulfate, Chem. Eng. J. 436 (2022).

[21] X. Wang, et al., Functionalized α-Al2O3 supported gold catalyst for photocatalytic oxidative esterification of benzyl alcohol with methanol to corresponding esters, J. Photochem. Photobiol. A Chem. (2024) 446.

[22] P. Munnik, P.E. de Jongh, K.P. de Jong, Recent developments in the synthesis of supported catalysts, Chem. Rev. 115 (14) (2015) 6687–6718.

[23] L. Fratalocchi, et al., A novel preparation method for "small" eggshell Co/γ-Al2O3 catalysts: a promising catalytic system for compact Fischer-Tropsch reactors, Catal. Today 246 (2015) 125–132.

[24] L. Usón, et al., VOCs abatement using thick eggshell Pt/SBA-15 pellets with hierarchical porosity, Catal. Today 227 (2014) 179–186.

[25] A.I. Moral-Rodríguez, et al., Removal of ronidazole and sulfamethoxazole from water solutions by adsorption on granular activated carbon: equilibrium and intraparticle diffusion mechanisms, Adsorption 22 (1) (2016) 89–103.

[26] B.F.K. Kingsbury, K. Li, A morphological study of ceramic hollow fibre membranes, J. Membr. Sci. 328 (1–2) (2009) 134–140.

[27] B.F.K. Kingsbury, Z. Wu, K. Li, A morphological study of ceramic hollow fibre membranes: a perspective on multifunctional catalytic membrane reactors, Catal. Today 156 (3–4) (2010) 306–315.

[28] A. Irankhah, et al., Fischer-Tropsch reaction kinetics of cobalt catalyst in supercritical phase, J. Nat. Gas Chem. 16 (2) (2007) 115–120.

[29] A.A.K. Reza Gheitanchi, Majid Taghizadeh, Yadollah Mortazavib, Effects of ceria addition and pre-calcination temperature on performance of cobalt catalysts for Fischer-Tropsch synthesis, React. Kinet. Catal. Lett. 88 (2006) 225–232.

[30] J. Fu, et al., Electrochemical activation of peroxymonosulfate (PMS) by carbon cloth anode for sulfamethoxazole degradation, Chemosphere 287 (2022) 132094.

[31] Y. Wang, et al., Natural polyphenols enhanced the Cu(II)/peroxymonosulfate (PMS) oxidation: the contribution of Cu(III) and HO•, Water Res. 186 (2020) 116326.

[32] J. Zheng, et al., A visible-light-driven heterojuncted composite WO(3)/Bi(12)O(17)Cl(2): Synthesis, characterization, and improved photocatalytic performance, J. Colloid Interface Sci. 510 (2018) 20–31.

[33] H. Koopi, F. Buazar, A novel one-pot biosynthesis of pure alpha aluminum oxide nanoparticles using the macroalgae Sargassum ilicifolium: a green marine approach, Ceram. Int. 44 (8) (2018) 8940–8945.

[34] S. Wang, J. Wang, Radiation-induced preparation of nanoscale CoO@graphene oxide for activating peroxymonosulfate to degrade emerging organic pollutants, Sci. Total Environ. 933 (2024) 173211.

[35] K.S. Kim, Y.J. Park, Catalytic properties of Co3O4 nanoparticles for rechargeable Li/air batteries, Nanoscale Res. Lett. 7 (1) (2012) 47.

[36] D.D.M. Prabaharan, et al., Precipitation method and characterization of cobalt oxide nanoparticles, Appl. Phys. A 123 (4) (2017).

[37] T. Song, et al., Fabrication of super slippery sheet-layered and porous anodic aluminium oxide surfaces and its anticorrosion property, Appl. Surf. Sci. 355 (2015) 495–501.

[38] T. Tago, et al., XPS study from a clean surface of Al2O3 single crystals, Procedia Eng. 216 (2017) 175–181.

[39] S. Zhang, et al., Enhanced permanganate oxidation of phenolic pollutants by alumina and potential industrial application, Water Res. 251 (2024) 121170.

[40] X. Li, et al., Influence of oxygen pressure and substrate temperature on the properties of aluminum fluoride thin films, Appl. Surf. Sci. 282 (2013) 226–230.

[41] R.-C. Fang, et al., High-performance bilayer flexible resistive random access memory based on low-temperature thermal atomic layer deposition, Nanoscale Res. Lett. 8 (1) (2013) 92.

[42] Q. Guo, et al., Co(3)O(4) modified polymeric carbon nitride for external light-free chlorine activating degradation of organic pollutants, J. Hazard. Mater. 429 (2022) 128193.

[43] J.P. Zou, et al., Electrochemical oxidation and advanced oxidation processes using a 3D hexagonal Co(3)O(4) array anode for 4-nitrophenol decomposition coupled with simultaneous CO(2) conversion to liquid fuels via a flower-like CuO cathode, Water Res. 150 (2019) 330–339.

[44] Y. Liu, et al., A versatile CeO(2)/Co(3)O(4) coated mesh for food wastewater treatment: simultaneous oil removal and UV catalysis of food additives, Water Res. 137 (2018) 144–152.

[45] X. Zhang, et al., Fenton-like membrane reactor assembled by electron polarization and defect engineering modifying Co(3)O(4) spinel for flow-through removal of organic contaminants, Water Res. 254 (2024) 121351.

[46] D. Pashchenko, Intra-particle diffusion limitation for steam methane reforming over a Ni-based catalyst, Fuel 353 (2023).

[47] X. Zhou, et al., Atomic cation-vacancy modulated peroxymonosulfate nonradical oxidation of sulfamethoxazole via high-valent iron-oxo species, Environ. Appl. Catal. B 330 (2023).

[48] C. Su, et al., Core-shell magnetic CFO@COF composites toward peroxymonosulfate activation for degradation of sulfamethoxazole from aqueous solution: a comparative study and mechanistic consideration, Chemosphere 311 (Pt 2) (2023) 137159.

[49] X.-L. Zou, H. Yan, X.-H. Chen, Evolution of second phases and mechanical properties of 7075 Al alloy processed by solution heat treatment, Trans. Nonferrous Met. Soc. Chin. 27 (10) (2017) 2146–2155.

[50] X. Xue, et al., Adsorption and oxidation of PCP on the surface of magnetite: Kinetic experiments and spectroscopic investigations, Appl. Catal. B 89 (3–4) (2009) 432–440.

[51] A.H. Asif, et al., Heterogeneous activation of peroxymonosulfate by Co-doped Fe(2)O(3) nanospheres for degradation of p-hydroxybenzoic acid, J. Colloid Interface Sci. 604 (2021) 390–401.

[52] R.A.K. Hirani, et al., Heterogeneous activation of persulfate by macroscopic nitrogen-doped graphene oxide cubes for the degradation of antibiotic contaminants in water, Sep. Purif. Technol. 319 (2023) 124110.

[53] R. Wang, et al., Non-radical mediated reduced graphene oxide/polypyrrole catalytic ceramic membrane-PDS system for source control of SMX, Chem. Eng. J. 479 (2024).

[54] J. Wang, S. Wang, Reactive species in advanced oxidation processes: Formation, identification and reaction mechanism, Chem. Eng. J. 401 (2020).

[55] W. Zhu, et al., MOFs-derived CuO-Fe(3)O(4)@C with abundant oxygen vacancies and strong Cu-Fe interaction for deep mineralization of bisphenol A, Environ. Res. 228 (2023) 115847.

[56] M. Xiong, et al., Efficient peroxymonosulfate activation by magnetic CoFe2O4 nanoparticle immobilized on biochar toward sulfamethoxazole degradation: performance, mechanism and pathway, Appl. Surf. Sci. 615 (2023).

[57] M. Lee, et al., Formation of micro-channels in ceramic membranes – Spatial structure, simulation, and potential use in water treatment, J. Membr. Sci. 483 (2015) 1–14.